

# Confirmation of Dynamically Recrystallized Grains in Hexagonal Zirconium through Local Internal Friction Measurements



K.S. THOOL, K.V. MANI KRISHNA, D. SRIVASTAVA, A. PATRA, R.D. DOHERTY, and I. SAMAJDAR

Fully recrystallized hexagonal Zirconium was subjected to controlled hot compression tests. Deformation above 723 K showed both flow saturation, characteristic of dynamic recovery, and also the presence of fine equiaxed grains, indicating dynamic recrystallization (DRx). Though data from relative work hardening were inconclusive, a combination of transmission Kikuchi diffraction plus transmission electron microscopy clearly confirmed the presence of DRx grains. A separation between the deformed and the DRx grains was not possible with microtexture or nano-indentation data. Local internal friction measurements (or  $\tan\delta$  values), however, clearly distinguished the DRx grains from both statically recrystallized (SRex) and the hot deformed grains.

<https://doi.org/10.1007/s11661-019-05412-9>

© The Minerals, Metals & Materials Society and ASM International 2019

## I. INTRODUCTION

HEXAGONAL Zirconium ( $\alpha$ -Zr) is used in the structural components in thermal nuclear reactors.<sup>[1,2]</sup> The actual components are typically fabricated through a series of hot and warm working steps followed by cold forming.<sup>[3,4]</sup> More specifically, the as-cast  $\alpha$ -Zr is subjected to forging or extrusion to break up the cast structure. This initial stage is followed by subsequent hot and warm extrusion to provide tubes for subsequent draw bench or pilgering and annealing. It is important to note that the microstructure and crystallographic texture obtained through warm-hot working is altered, though not very significantly, during the final cold working plus annealing stages.<sup>[5]</sup>

The warm/hot working of Zr may occur in single-phase bcc-Zr ( $\beta$ -Zr), but also as  $\alpha + \beta$ -Zr and as  $\alpha$ -Zr.<sup>[6,7]</sup> Lower working temperatures have the specific advantage in improved dimensional tolerance.<sup>[8]</sup>

However, it typically involves higher loads. Working at higher temperatures, to take advantage of the lower loads, leads to either a saturation of the flow stress or often an actual fall. Classical text books<sup>[9,10]</sup> and review articles,<sup>[11,12]</sup> mainly based on studies of cubic alloys, attributed the former to dynamic recovery; while flow softening was related to dynamic recrystallization (DRx).<sup>[13]</sup> During dynamic recovery, the original grain structure undergoes a change in shape as determined by the strain imposed. The DRx, on the other hand, involves formation of initially strain-free and usually equiaxed grains. The high-temperature deformation involves complex interplay between dynamic recovery and DRx. For example: extended recovery, often observed in fcc metals with high stacking fault energy, inhibits DRx and leads to flow stress saturation. The fcc metals with lower stacking fault energy, on the other hand, undergo DRx and show flow softening after an early peak flow stress.

Most reviews of hot deformation<sup>[10,14,15]</sup> related DRx with flow softening and corresponding appearance of an inflection in the stress dependence of strain hardening, that is  $d^2\theta/d\sigma^2 = 0$ ,<sup>[15,16]</sup> where  $\sigma$  is true stress,  $\epsilon$  is true strain, and  $\theta$  represents  $d\sigma/d\epsilon$ .  $d^2\theta/d\sigma^2 = 0$  is observed prior to the peak stress that corresponds to the formation of a significant fraction of the recrystallized grains. The origin of 'new' grains in hot deformed microstructures was related to various processes: continuous DRx,<sup>[17]</sup> geometric DRx,<sup>[18–20]</sup> and for flow softening to standard discontinuous DRx.<sup>[21,22]</sup> In the later, regions are swept by the migration of high-angle boundaries creating the new equiaxed grains. Such new

---

K.S. THOOL, A. PATRA, and I. SAMAJDAR are with the Metallurgical Engineering and Material Science Department, Indian Institute of Technology-Bombay, Powai, Mumbai 400076, India. Contact e-mail: [indra@iitb.ac.in](mailto:indra@iitb.ac.in) K.V. MANI KRISHNA is with the Materials Science Division, Bhabha Atomic Research Centre, Trombay, Mumbai 400085, India. D. SRIVASTAVA is with the Nuclear Fuel Complex, Hyderabad 500062, India. R.D. DOHERTY is with the Metallurgical Engineering and Material Science Department, Indian Institute of Technology-Bombay and also with the Department of Materials Science and Engineering, Drexel University, Philadelphia PA 19104.

Manuscript submitted April 2, 2019.

Article published online August 22, 2019

recrystallized grains initially have very low dislocation density, in which the local resistance to plastic deformation is low. These soft regions allow the imposed strain to be achieved at reduced flow stress, thus accounting for the observed flow softening.

In a recent study by Luan *et al.*,<sup>[17]</sup> fine equiaxed grains, the classical signature of DRx, were observed in warm/hot deformed  $\alpha$ -Zr. In certain orientations, the DRx was associated with flow saturation and no indication of work softening was noted. The appearance of DRx grains, in hot deformed  $\alpha$ -Zr, with only flow saturation<sup>[17,19]</sup> is an unexpected result. And this formulated the twin objectives of the present manuscript (i) to establish the presence of potential DRx grain in warm/hot compressed  $\alpha$ -Zr and (ii) to identify the microstructural origin for such grains.

This manuscript thus involved hot compression of  $\alpha$ -Zr in a deformation simulator. Associated flow behavior and microstructures were critically analyzed with respect to the working temperature. Deformation above 723 K showed flow saturation and clear presence of fine equiaxed grains. The microstructures were then explored, by combinations of microtexture measurements and local mechanical responses, to identify the microstructural origin of these fine equiaxed grains.

## II. EXPERIMENTAL METHODS

A commercial Zircaloy-4 (chemical composition listed in Table I) was obtained as hot extruded bar. This was then cold rolled, in a laboratory rolling mill, to 50 pct reduction in thickness. The cold rolled plate was annealed (at 1033 K for 6 hours). This provided a fully recrystallized microstructure with an average grain size of 50  $\mu\text{m}$ . From the mid-width and mid-thickness sections of the rolled and annealed plate (of  $\sim 15$  mm thickness), cylindrical compression specimens of 8 mm diameter and 12 mm length were fabricated. As shown in Figure 1, two types of specimens (A and B) were made. The specimens naturally had different crystallographic textures with respect to the compression axis. The samples were then subjected to controlled uniaxial compression in a deformation simulator (Gleeble-3800<sup>TM</sup>). The compression tests were conducted to a 40 pct reduction in thickness (strain rate of 0.005  $\text{s}^{-1}$ ), followed by water quenching. Gleeble<sup>TM</sup> data were analyzed to obtain stress-strain and work hardening plots. Deformation were also undertaken at different strain rates and values of temperature-dependent activation energy for plastic deformation were estimated using an established protocol.<sup>[23]</sup>

Post warm/hot compression, specimens were sectioned (using slow-speed diamond cutting) in two equal halves parallel to the compression axis. The surfaces were then prepared with standard metallographic polishing, followed by electropolishing. An electrolyte of 80:20 methyl alcohol and perchloric acid was used at 253 K and 20 volts dc. The electropolished specimens were then subjected to various structural characterizations. These included EBSD (electron backscattered diffraction with TSL-OIM<sup>TM</sup>) measurements in a

FEI<sup>TM</sup> Quanta 3D-FEG (field emission gun) SEM (scanning electron microscope). It is to be noted that only measurement points with confidence index or CI > 0.1 were used for data analysis and interpretation. Data with CI < 0.1 were treated as non-indexed, and were shown as 'black' points in the respective EBSD images. In addition to standard mapping and grain size estimation (by area), EBSD data were also analyzed for grain interior misorientations: GOS (grain orientation spread) and GAM (grain average misorientation). For both of them, a grain definition was needed. A grain was defined as a region bound by > 5 deg boundaries. The average grain orientation ( $g_{av}$ ) was taken as a quaternion average. GOS represented average misorientation of all measurement points, within a grain, from the  $g_{av}$ . GAM, on the other hand, provided point-to-point misorientation within a grain. Mathematically, these are defined<sup>[24-26]</sup> as,

$$\text{GOS} = \frac{1}{N} \sum_{i=1}^N g_{av} g_i^{-1} \quad [1]$$

$$\text{GAM} = \frac{1}{N} \sum_{i=1}^N \left[ \sum_{i,j=1}^{nm} (g_i g_j^{-1}) \right] \quad [2]$$

where  $g_{av}$  is the quaternion average of a grain orientation. The grain contains  $N$  data points of  $g_i$  ( $i = 1$  to  $N$ ) orientations.

Additionally, TEM samples were also prepared (using the same electrolyte and polishing condition, in a twin-jet electropolisher: Struers<sup>TM</sup> Tenupol-5). They were used for transmission Kikuchi diffraction (TKD)<sup>[27]</sup> and transmission electron microscopy (TEM: Jeol<sup>TM</sup> 2010, operated at 200 keV). Site-specific nano-indentation<sup>[28]</sup> and nano-dma (dynamic mechanical analysis) were conducted on the electropolished specimens using a Hysitron<sup>TM</sup> PI-87 unit (in the same SEM). For the nano-indentation, a load of 1000  $\mu\text{N}$ , with standard quasi-static trapezoid load function, was used.  $\tan\delta$  values were estimated from the nano-dma measurements. Nano-dma measurements were made at ambient temperature within a frequency range of 5 to 150 Hz. A contact load of 700  $\mu\text{N}$  plus an oscillating 30  $\mu\text{N}$  load were used. Site-specific nano-indentation is not an uncommon technique, the reader may refer elsewhere for further details.<sup>[29,30]</sup> Site-specific internal friction measurements are, however, less common, with limited literature<sup>[31-33]</sup> available on the subject. Bulk texture and dislocation density measurements were carried out with X-ray diffraction in a Bruker<sup>TM</sup> D8 Discover X-ray diffraction unit. An area detector, Vantec<sup>TM</sup>, was used for these measurements using  $\{01\bar{1}0\}$ ,  $\{0002\}$ ,  $\{01\bar{1}1\}$ ,  $\{01\bar{1}2\}$ , and  $\{11\bar{2}0\}$  poles. For details, on such measurements with area detector signal, the reader may refer elsewhere.<sup>[34]</sup> For ODF (orientation distribution function) calculations, a commercial software Labosoft<sup>TM</sup> was used. Three-dimensional ODFs<sup>[35]</sup> were plotted using another commercial software: slicer-dicer<sup>TM</sup>. Dislocation densities were measured from the X-ray line profiles using fourth-order moment.<sup>[36]</sup>

**Table I. Chemical Composition of Zircaloy-4 Used in the Present Study**

Element	Sn	Fe	Cr	Al	Hf	C	Zr
Amount by Weight Percentage (Pct) or Parts Per Million (ppm)	1.32 pct	0.2 pct	0.1 pct	39.0 ppm	< 50 ppm	< 55 ppm	balance

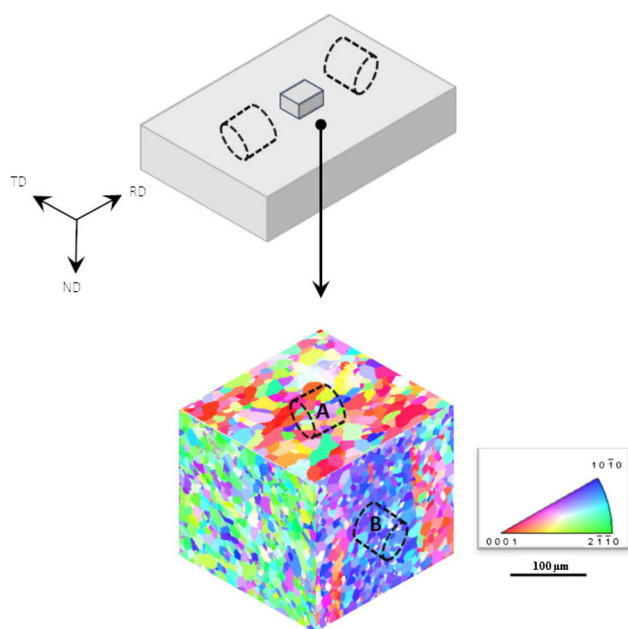


Fig. 1—The schematic of the starting cold rolled + annealed plate and electron backscattered diffraction (EBSD) inverse pole figure (IPF) maps of different cross-sections. Cylindrical compression specimens of two different orientations (marked as A and B) were prepared from the fully recrystallized plate.

### III. RESULTS

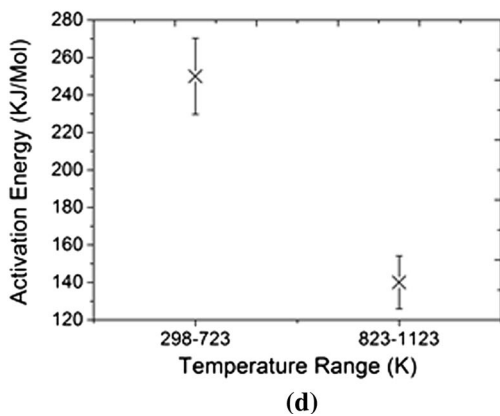
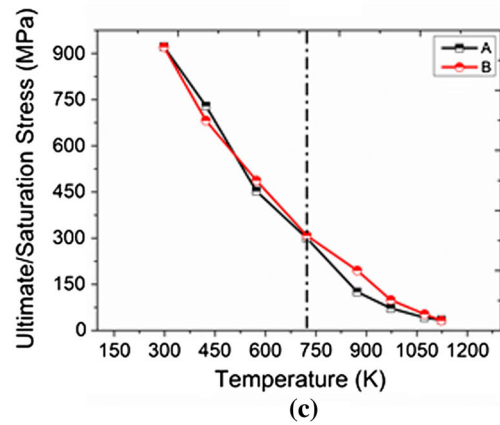
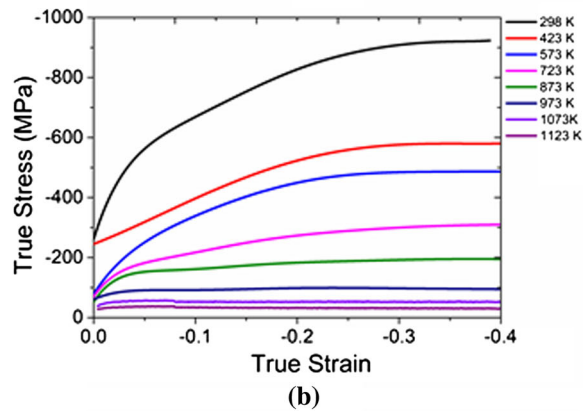
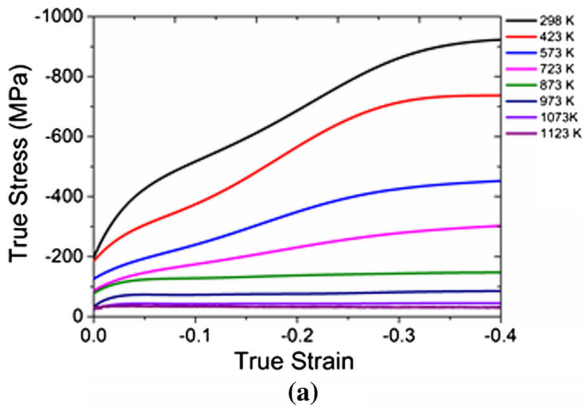
From the cold rolled + annealed Zircaloy-4 plate, compression specimens of two different orientations (described as A and B, see Figure 1) were produced. It is to be noted that the starting recrystallized structure was not homogeneous. It had, at certain locations, visible banding of similar crystallographic orientations (texture banding). This can be attributed to a combination of preferred nucleation plus growth inhibition during static recrystallization of cold deformed single-phase Zr.<sup>[37]</sup> However, as the scope of the present study was to explore DRx, this aspect of statically recrystallized microstructure is not investigated further.

The Zircaloy-4, used in this manuscript, is expected<sup>[5]</sup> to remain 100 pct hexagonal ( $\alpha$ ) under the deformation temperatures involved. This was also confirmed by standard dilatometry. The true stress ( $\sigma$ ) vs true strain ( $\epsilon$ ) plots of the  $\alpha$ -Zr deformed at different temperatures (298 K to 1123 K) are given in Figures 2(a) and (b) for samples A and B, respectively. The stress-strain plots appeared to indicate two different warm/hot working responses. Deformation from 298 K to 723 K led to extended work hardening, while work hardening saturated after strains of less than 5 pct for compressions at

$T > 723$  K. More specifically,  $T > 723$  K hot compression showed flow saturation but not flow softening.

Further exploration of the flow curves brought out two additional points. Firstly, the saturation ( $> 723$  K) or ultimate compressive ( $723$  K  $<$ ) strength dropped nearly monotonically with working temperature (Figure 2c). There was no clear discontinuity above and below 723 K working. However, the estimated (for details of the analysis, see<sup>[23]</sup>) activation energy ( $Q$ ) of plastic deformation (see Figure 2(d)) were remarkably different. For hot compression at  $T \leq 723$  K, the estimated mean  $Q$  value was 250 kJ/mole (a range of 237 to 269 kJ/mole). Above 723 K hot compression, on the other hand, provided a significantly lower  $Q$  of 140 kJ/mole (a range of 124 to 151 kJ/mole). As suggested by Bourell and McQueen,<sup>[7]</sup>  $\sim 2$  times change in the  $Q$  may indicate possible changes in the deformation mechanism. However, an alternate explanation is also possible. Activation energy of diffusion in  $\alpha$ -Zr, below  $\sim 923$  K, approaches 275 to 350 kJ/mol.<sup>[20,38]</sup> However, this drops to as low as 90 to 115 kJ/mol at high temperatures. Such a remarkable change appears to be related to the ultra-fast diffusion of impurities (example: trace amounts of iron).<sup>[39,40]</sup> Despite this estimated change in activation energy, the measured values of the self-diffusion coefficient in  $\alpha$ -Zr show no discontinuity at  $\sim 923$  K. In other words, the changes in the activation energy for hot deformation (Figure 2(d)) appear to arise in terms of the temperature dependence of self-diffusion and not from changes in the deformation mechanism. These points are discussed further in the discussion section.

The motivation of this manuscript was to identify possible dynamic recrystallization (DRx) in  $\alpha$ -Zr. The presence of DRx is often reflected<sup>[10,14,15]</sup> on the work hardening behavior, and the same was extracted from the experimental flow curves. As shown in Figure 3(a), till 873 K deformation, and for both specimens A and B, significant increases in the work hardening rate were observed in the  $\frac{d\sigma}{d\epsilon}$  vs  $\sigma$  plots. Literature related such increase (or inflection) in fcc metallic materials as stages IIIA and IIIB.<sup>[38]</sup> These are also reported in  $\alpha$ -Zr,<sup>[41,42]</sup> and they typically arise from deformation twinning. More specifically, deformation twinning can give an increase, or a reduction in the rate of fall, in strain hardening rate with increased strain. Deformation twinning thus appears as a likely mechanism to account for the increase in strain hardening observed at the lower deformation temperatures ( $T \leq 723$  K) in Figure 3(a). The magnitude of the twinning-induced strain hardening was greater in sample A. This variation can plausibly be attributed to the differences in crystallographic texture.<sup>[43]</sup>



◀ Fig. 2—True stress ( $\sigma$ ) vs true strain ( $\epsilon$ ) plots (for different working temperatures) of compression specimens (as in Fig. 1) (a) A and (b) B. The specimens were compressed to a maximum true strain of 0.4. (c) Saturation stress (or the ultimate compressive strength) of specimens A and B vs working temperature. (d) Activation energy of plastic deformation vs working temperature for both specimens (A and B). It showed significant lowering of the activation energy in the 823 K to 1123 K temperature range.

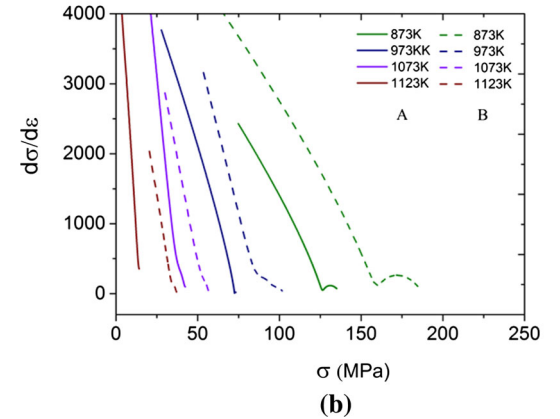
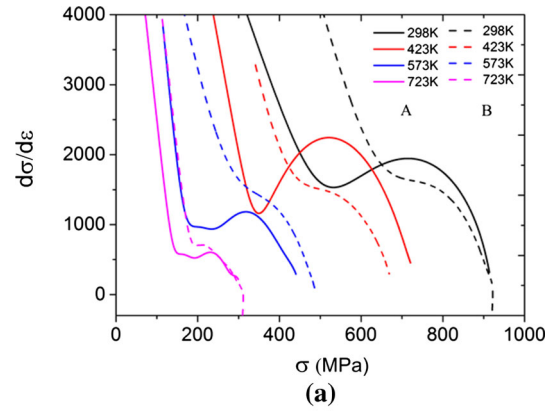


Fig. 3—Work hardening behavior ( $\frac{d\sigma}{d\epsilon}$  vs  $\sigma$ ) for both specimens (A and B) at (a) 298 K to 723 K and (b) 823 K to 1123 K.

Later in this manuscript, clear experimental evidence of deformation twinning in Zirconium was presented at temperatures as high as 873 K, which is 0.41 of the melting temperature ( $T_M$ ). However, this is not surprising and appears consistent with the published literature.<sup>[17,44]</sup> More significantly for this manuscript,  $T > 723$  K deformation showed flow saturation, with no sign of the flow softening. For  $T > 823$  K, there was a consistent absence of the twinning-related inflection and corresponding increase in the strain hardening rate. The small strain hardening inflections, seen at 723 K (Figure 3(a)) and 823 K (Figure 3(b)), are characteristic of the so-called Stage IV of dislocation hardening.<sup>[45]</sup> This transition is commonly associated with the role of dislocation dipoles produced by dynamic recovery. Stage IV is expected to vanish at higher temperatures by thermally activated dislocation climb, which eliminates dislocation dipoles.

The expected inflection point, in warm worked metallic materials, associated with the first onset the DRx<sup>[10,14,15]</sup> should show a *decrease* in strain hardening preceding the onset of work softening. Hence, it is expected that the actual decrease in strain hardening, associated with a maximum or peak in flow stress, occurs with a significant volume fraction of new soft DRx grains.<sup>[16]</sup> In other words, the flow behavior (Figures 2(a), (b), and 3(a), (b)) showed no sign of the work softening response usually characteristic of noticeable DRx.

Microstructural evolution, for the entire range of deformation temperatures, is shown in Figures 4(a) and (b). The figures show, for both specimen orientations (samples A and B), a remarkable difference in the temperature-dependent deformed microstructure evolution. Up to and including 723 K, the microstructures comprised of deformed grains and fragmented regions. The latter was seen in the EBSD scans as non-indexed points or regions. These were regions with below 0.1 confidence index (CI). CI is a measure of accuracy in automated indexing: CI > 0.1 representing > 95 pct accuracy.<sup>[46]</sup> In the subsequent section (on Discussion), the subject of fragmented and non-fragmented grains<sup>[47]</sup> is discussed further. In the present section, it is important to appreciate a clear transition in the deformed microstructure. Above 723 K the fragmented regions, indicated by low CI regions, were greatly reduced. For T ≥ 873 K, clear presence of fine (1 to 5 μm in size) equiaxed grains were observed. At 873 K deformed microstructure, for example (Figure 4(c)), showed nominal presence of non-indexed points (they were present mostly at the grain boundaries). However, both fine equiaxed grains (albeit a few in number) and clear deformation twins (compression twin with 90 deg ⟨1120⟩ orientation relationship) were present. Much of the later analysis concentrates on the identification of the nature and origin of the fine equiaxed grains seen in Figures 4(a) and (b).

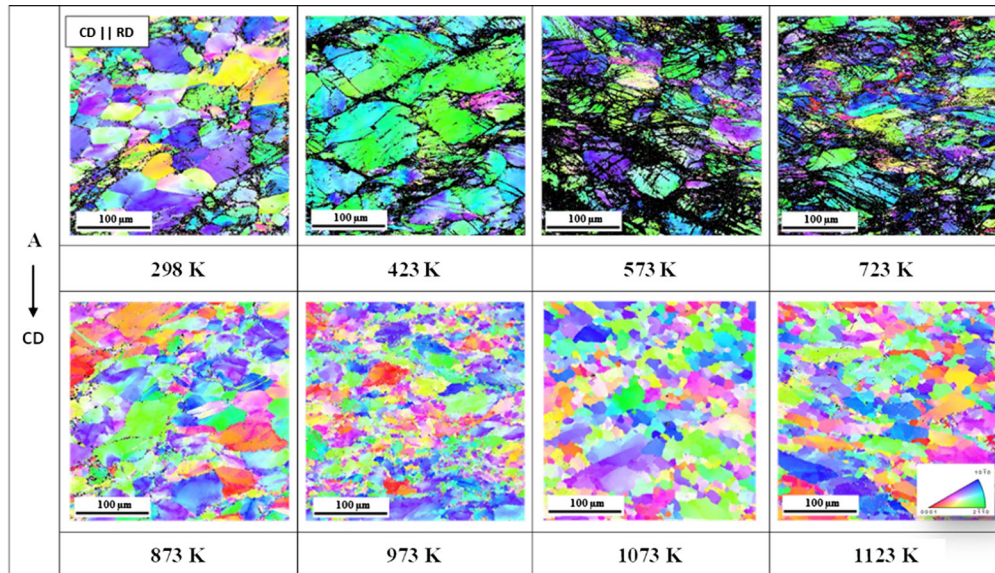
The clear appearance of the fine equiaxed grains did not conclusively reflect on the overall microstructural analysis (Figures 5(a) through (c)) and on the X-ray line profiles (Figure 5(d)). As shown in Figure 5(a), the fraction of data points with CI < 0.1 (the non-indexed points indicating fragmented regions<sup>[47]</sup>) increased with working temperatures: reaching a saturation at ~ 573 K. Indexing improved, that is the frequency of low CI points fell, beyond 723 K. This correlated with the appearance of the fine equiaxed grains. The average area fraction of 1 to 5 μm grains (or the fine equiaxed grains) were essentially constant, at ~ 0.025, till 723 K. A similar number was noted in the undeformed specimen as well. That fraction of apparent fine grains, in both as recrystallized and lightly deformed structures, is expected to arise from the existence of some grains of that size and also from sectioning larger grains near their corners. The area fraction of 1 to 5 μm grains, however, increased > 723 K deformation: reaching a maximum at 973 K, and then finally falling at higher deformation temperatures. High-angle boundary fraction, an important parameter often used in identifying

the DRx grains,<sup>[14,48,49]</sup> was largely unchanged (within experimental scatter) till 723 K. It, however, showed a noticeable increase above 723 K. This increase in the fraction of high-angle grain boundaries also correlated with the formation of the fine equiaxed grains at higher deformation temperatures.

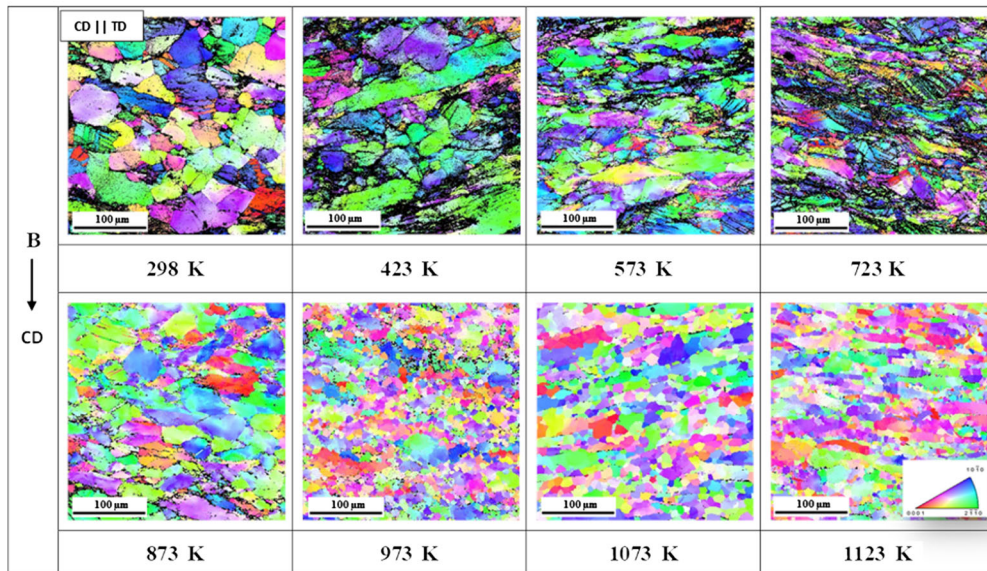
Dislocation densities were measured from the X-ray line profiles using data from an area detector (Vantec<sup>TM</sup>). Normalized dislocation density ( $\rho_N$ : dislocation density of the deformed specimen normalized by the dislocation density of the recrystallized structure) was then evaluated as a function of deformation temperature for different X-ray peaks. Figure 5(d) presents the data on  $\rho_N$  for the basal (0002) pole, where  $\rho_N$  had a maximum of ~ 10<sup>7</sup> (times of the fully recrystallized state) at lower deformation temperatures. Beyond 573 K deformation  $\rho_N$  had undergone a steady drop, reaching a minimum of ~ 10<sup>2</sup> (times of the fully recrystallized state) at and beyond 973 K. Similar trend was noted for the non-basal poles as well. This fall in dislocation density with increasing deformation temperature is an expected result, indicating that the dominant softening mode to be thermally assisted dynamic recovery. Any extra softening by partial DRx appears well hidden, although the visible fraction of the suspected DRx reached an area fraction of ~ 0.25 at 973 K (see Figure 5(b)). In other words, the flow data (Figures 2 and 3) and much of the microstructural evidence (Figure 5) indicated a major role of dynamic recovery in the softening behavior. The softening through DRx, albeit with a limited area fraction of suspected DRx grains (Figures 4 and 5(c)), did not appear to be significant.

Changes in the bulk crystallographic texture (Figure 6) also appeared gradual and did not significantly differ with the appearance of fine equiaxed grains. Figure 6(a) shows the three-dimensional orientation distribution function (ODF)<sup>[50]</sup> plots for the two selected deformation temperatures: 573 K and 973 K (for brevity, all ODFs are not included). The starting material had a basal texture: with clear peaks at selective crystallographic orientations ( $\phi_1 = 90$  and 270 deg in sample A and  $\phi_1 = 0$  and 180 deg in sample B, along the constant  $\phi_2 = 0$  deg and 60 deg sections). 423 K deformation strengthened these components, while deformation at higher temperatures enhanced the orientation spread and weakened the above-mentioned texture components. The last point is also captured with texture index values (see Figure 6(b)). Texture index, a representation of overall anisotropy due to crystallographic texture,<sup>[50]</sup> enhanced clearly till 423 K compression. Beyond 423 K, however, a steady drop of texture index was clearly noted.

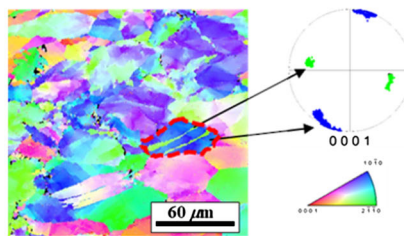
The non-indexed points (measurement points below CI < 0.1) may also have preferred crystallographic orientations. The latter may come from orientations with higher defect concentration and/or possible orientation effects on indexing.<sup>[51]</sup> This can be addressed by appropriate data partitioning plus clean-up. However, this was not carried out in this study. Following were the reasons: (i) any clean-up, except for newly emerging



(a)

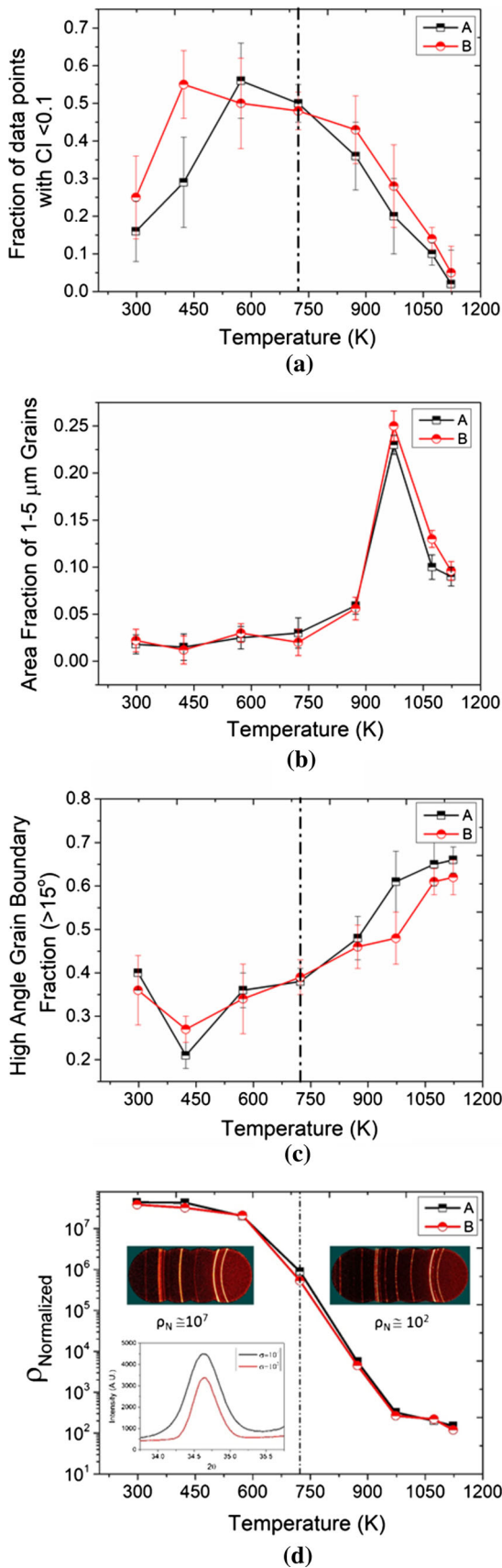


(b)



(c)

Fig. 4—EBSD-IPF maps of specimen (a) A and (b) B. These were tested at different temperatures, and a maximum true strain of 0.4, and then water quenched. The microstructures revealed the presence of fine (1 to 5  $\mu\text{m}$ ) equiaxed grains for specimens deformed at 823 K to 1123 K. (c) EBSD, with finer step size, showing the presence of compression twins (90 deg  $\langle 11\bar{2}0 \rangle$ ) and few fine equiaxed (1 to 5  $\mu\text{m}$ ) grains in a 873K compressed specimen. Black points in the respective EBSD images represent regions with below 0.1 confidence index (CI). CI is a statistical measure of the accuracy of automated indexing Ref. [44]; indexing with CI > 0.1 represents > 95 pct accuracy.



◀ Fig. 5—(a) Fraction of data points with confidence index (CI) < 0.1, (b) area fraction of 1 to 5  $\mu\text{m}$  grains, and (c) number fraction of > 15 deg boundaries. (d) Normalized dislocation density ( $\rho_N$ : absolute dislocation density normalized by the dislocation density in the annealed specimen) for (0002) pole. In (d), area detector image plus corresponding peak profiles for the two extremes  $\rho_N$  are included. All figures are plotted as a function of working temperatures in specimens A and B. All plots include a dotted line at 723 K: temperature demarcating clear changes (see Fig. 4) in the microstructure.

techniques like NPAR<sup>TM</sup> [52] has potentials for affecting data integrity and (ii) the ‘limited’ EBSD scan areas were inappropriate for quantitative texture analysis.

The fine equiaxed grains, a critical feature in the temperature-dependent microstructure evolution (Figure 4), may originate from dynamic or meta-dynamic recrystallization. [15] Possibilities of static recrystallization also cannot be completely ruled out. It is to be noted that samples were water quenched ( $\sim 500$  to  $600$  K/s cooling rates were typically achieved in the Gleeble<sup>TM</sup>) immediately after the warm/hot compression tests. The ultra-fast cooling reduced the possibility of post-deformation static recrystallization. A combination of Transmission Kikuchi Diffraction (TKD) and Transmission Electron Microscopy (TEM), see Figure 7, was, however, effective in providing microstructural insights on the fine equiaxed grains. In Figure 7(a), such grains often appeared around large deformed grains. With EBSD-IPF maps, it was impossible to pinpoint their nature. However, high-resolution TKD (5 nm step size) plus TEM clearly showed (Figures 7(b) and (c)) the presence of significant orientation gradients (relative misorientation around a mean or average orientation) and of dislocations inside such grains. That is, TKD + TEM clearly identified that plastic deformation was present in these new, high temperature, fine (1 to 5  $\mu\text{m}$  size) equiaxed grains. This is of course expected only for DRx. No such features of plastic deformation would be expected in statically recrystallized grains, which are formed after the termination of plastic deformation.

Efforts were also made to identify the DRx grains from their grain interior misorientations and site-specific mechanical properties. The former is characterized as either grain orientation spread, GOS, and grain average misorientation GAM. It is to be noted that GOS increases with grain size ‘d’. [53] Figure 8(a) thus plots GOS/d values for two distinct microstructural entities: grains above and below 5  $\mu\text{m}$  in size. The values from the statically recrystallized (SRex) grains, from the sample before hot deformation, are also included for comparison. This exercise was also repeated for GAM (Figure 8(b)). The grain interior misorientations (Figures 8(a) and (b)) showed overlap between different microstructural features. In other words, it appears that grain interior misorientations may not be used as definite evidence for the fine equiaxed grains being a product of the DRx. These measurements, though not conclusive, are still clearly consistent with the DRx origin of the fine grains. Site-specific nano-indentation measurements

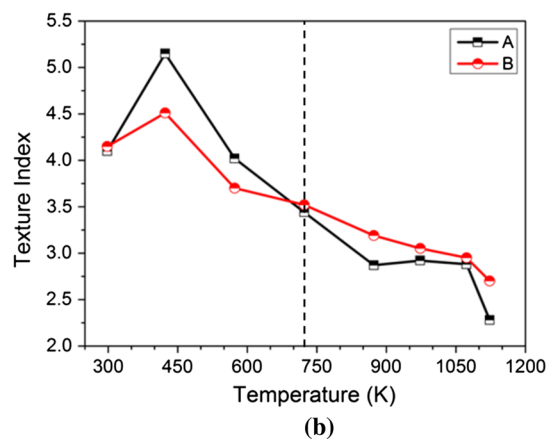
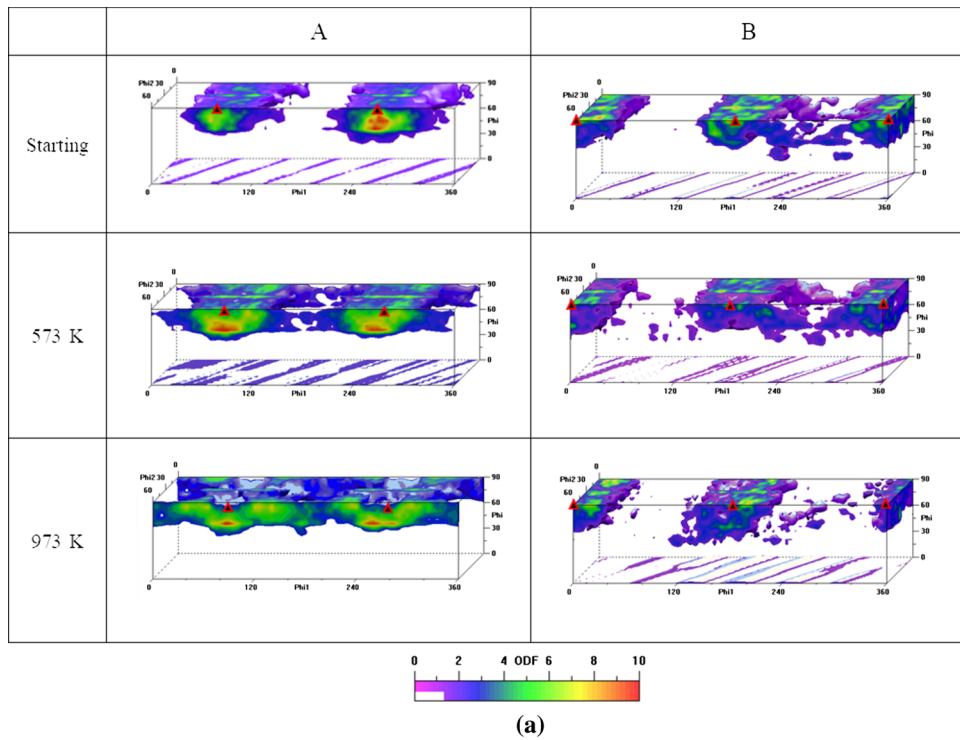
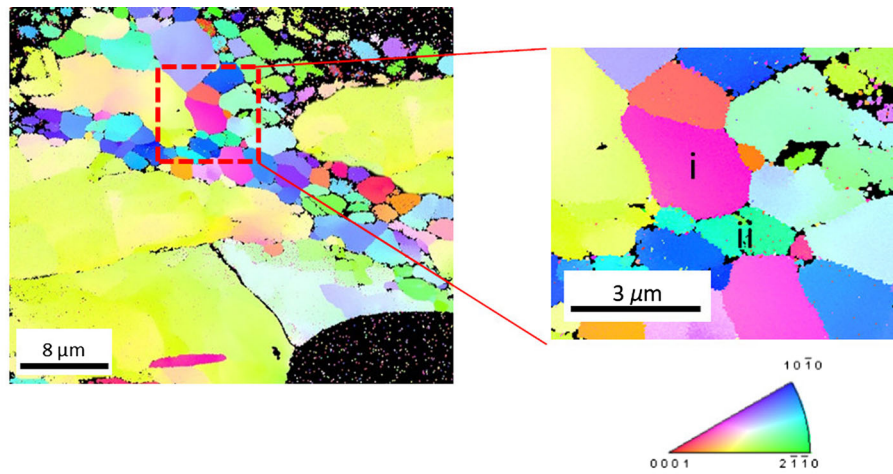


Fig. 6—(a) X-ray orientation distribution function (ODF) for the starting materials and specimens deformed at 573 K and 973 K. (b) Texture index vs working temperature. In (b) a dotted line indicates 723 K—temperature demarcating clear changes (see Fig. 4) in the microstructure.

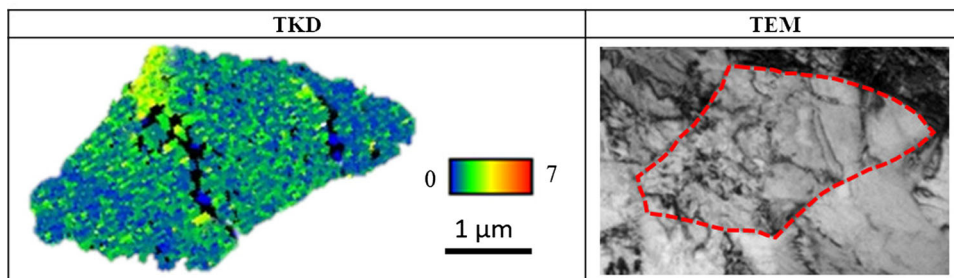
were also conducted. The hardness of hexagonal Zirconium strongly depends on crystallographic orientation.<sup>[54]</sup> Hence, this study used at least 10 grains (from each microstructural feature): each within 10 deg of either (0002) (Figure 9(a)) or (11 $\bar{2}$ 0) (Figure 9(b)) plane normal. Though 1 to 5  $\mu\text{m}$  grains had higher hardness than the SRex grains, the hardness difference between 1 and 5  $\mu\text{m}$  and > 5  $\mu\text{m}$  grains had a clear overlap. Arguably, the average hardness of the small DRx grains was somewhat less than that of the large deformed grains. However, this can also be attributed to the Hall–Petch effect.<sup>[55]</sup> It is to be noted that the DRx grains also had smaller size than the SRex or the deformed grains. In summary, like the grain interior misorientation data, the hardness values are inconclusive of the DRx origin for the fine equiaxed grains.

EBSD measurements with smaller step size (100 nm—see Figure 10) covered significantly smaller area. However, they brought out finer details. For example, they showed two types of fine equiaxed grains. Based on the spatial location, they were generalized as ‘\*’ and ‘+,’ respectively. The \* grains were observed at the boundaries of large deformed grains, and they had low-angle (1 to 15 deg) boundaries with the suspected parent grain (P). They, however, shared high-angle boundaries (> 15 deg) with the deformed neighboring grains into which they appeared to be growing. It thus appeared that strain-induced boundary migration (SIBM)<sup>[56,57]</sup> was associated with their formation. The + grains, on the other hand, had the classical necklace structure. It may be argued that the SIBM started with the ‘\*’ grains. The necklace grains, on the other hand, are expected to form

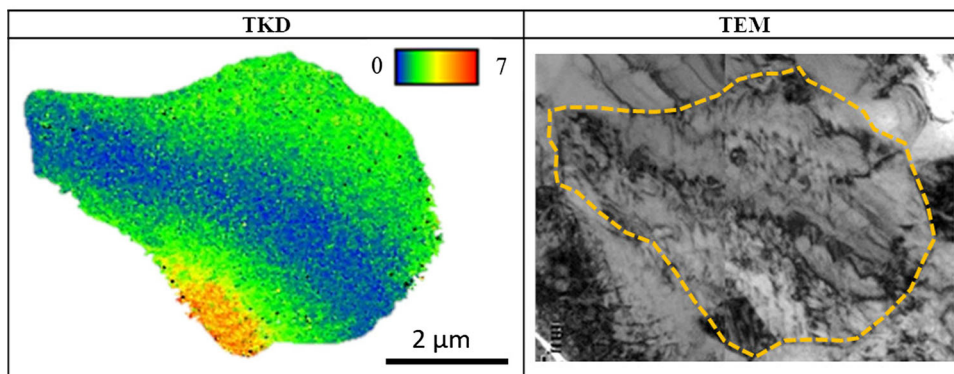




(a)



(b)



(c)

Fig. 7—(a) Transmission Kikuchi Diffraction (TKD) IPF map of specimen A deformed at 973 K. The microstructure shows clear presence of fine (1 to 5  $\mu\text{m}$ ) equiaxed grains. Two of these grains (i) and (ii) in (a) were subjected to high-resolution (5 nm step size) TKD and are shown in (b) and (c) along with their TEM images. The TKD images showed orientation gradients, while TEM showed the presence of dislocation.

by repeated SIBM, deformation-induced rotations, further contributing to their orientation development. The latter may also explain their greater orientation spreads, see Figure 10.

Microtexture data, on grain interior misorientations (as in Figure 8), or location-dependent nano-indentations (as in Figure 9) could not distinguish between the suspected DRx grains (\* and + grains in Figure 10) with the deformed grains or with the statically recrystallized (SRex) grains. This is not surprising. The necklace grains, in an earlier study,<sup>[37,58]</sup> were shown

to possess both high (as in a typical deformed grain) and low (similar to a recrystallized grain) grain interior misorientations. In summary, though the direct experimental results showed (see Figure 7) the presence of fine equiaxed grains, their clear demarcation (from other microstructural features) was not yet fully established (especially from the misorientation distributions and the nano-indentation measurements).

In order to explore the possibility of finding a definite method of discrimination, between different microstructural features (as in Figure 10), local dynamic

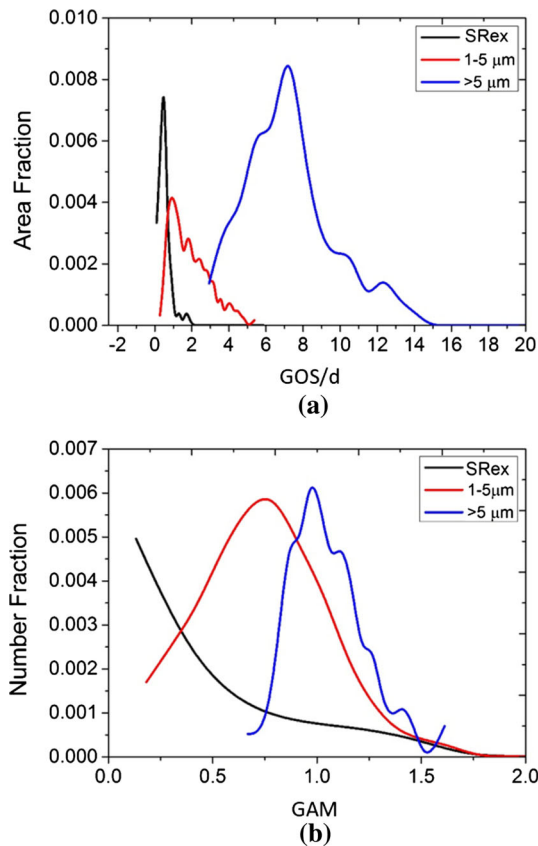


Fig. 8—Number fraction vs (a) GOS/d (grain orientation spread normalized by grain size) and (b) GAM (grain average misorientation). These are shown for statically recrystallized grains (SRex), and 1 to 5 (fine equiaxed grains) and > 5  $\mu\text{m}$  grains. The last two features were from specimen A after 973 K hot compression. Similar observations were valid for other deformation conditions as well.

mechanical analyses (dma) were performed. As shown in Figure 11(a), nano-dma measurements of  $\tan\delta$  were sensitive to imposed ‘minor’ plastic strain, of  $\sim 5$  pct tensile elongation, in a surface grain. Nano-dma,  $\tan\delta$ , also showed a reproducible and clear distinction between the different microstructural features, see Figures 11(b) and (c). It is to be noted, as discussed further subsequently (discussion section), that multiple relaxation peaks, attributed to specific events, have been identified in metallic materials.<sup>[59,60]</sup> The research articles related such relaxation events and possible mechanism(s) involved.<sup>[61,62]</sup> Within the narrow frequency range (5 to 150 Hz), which did not delineate a specific relaxation peak, the deformed grains had higher  $\tan\delta$  than the small DRx grains. The SRex grains, on the other hand, clearly had the lowest  $\tan\delta$  values. The current results (Figure 11) thus provide a clear, and novel, means of distinguishing discontinuous DRx grains using localized internal friction measurements.

#### IV. DISCUSSION

As described elsewhere,<sup>[63,64]</sup> plastic deformation in single-phase hexagonal Zirconium often shows extreme

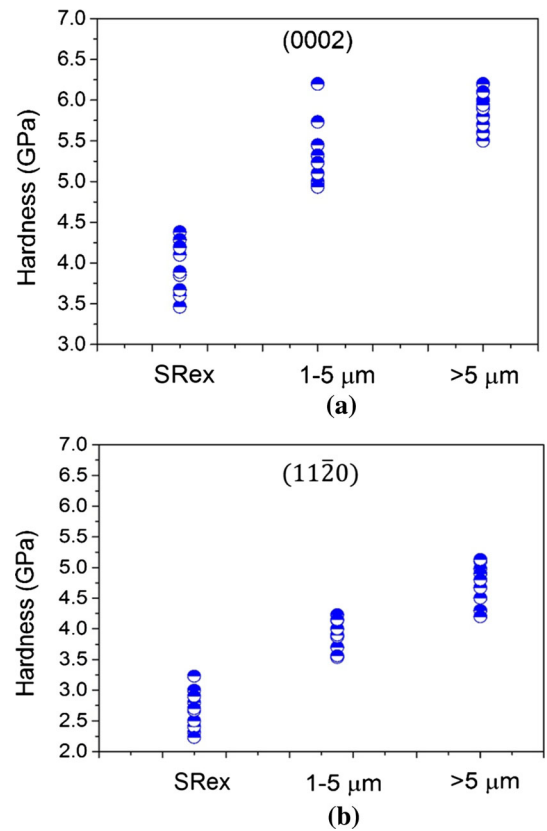


Fig. 9—Pico hardness measurements for (a) Basal (0002) and (b) Non-Basal (11 $\bar{2}$ 0) orientations. These are shown for statically recrystallized grains (SRex), 1 to 5  $\mu\text{m}$  (fine equiaxed grains) and > 5  $\mu\text{m}$  (deformed grains) grains. All measurements were taken after 973 K hot compression in specimen A and for regions within 10 deg of ideal (0002) and (11 $\bar{2}$ 0). Similar observations were valid for other deformation conditions as well.

strain partitioning.<sup>[65]</sup> Grains, or part of the deformed grains, may experience significant near-boundary mesoscopic shear strains.<sup>[47]</sup> Such grains or regions naturally undergo severe fragmentation. The latter was captured, even with moderate strain deformation, as the non-indexed points (displayed as black pixels in the EBSD images of Figures 4(a) and (b)). It is indeed interesting, and unexpected, that the frequency of non-indexed points increased with working temperature and then dropped (see Figure 5(a)). The latter is expected since higher deformation temperatures allow more dynamic recovery. The unexpected increase in non-indexed points and misorientation with the initial increase in deformation temperature have been previously reported.<sup>[65]</sup> Though a clear numerical model was not presented, the phenomenon (more misorientation at slightly higher working temperature) was attributed to activation of additional slip system(s). Increased dynamic recovery by higher temperature deformation was confirmed by the dislocation density measurements (see Figure 5(d)). The  $\rho_N$  showed a very rapid fall above 723 K. 723 K compression, however, did not show noticeable presence of fine equiaxed grains (Figure 5(b)). The latter was observed only for deformation at  $T \geq 873$  K. Discontinuous DRx was naturally suspected for these fine

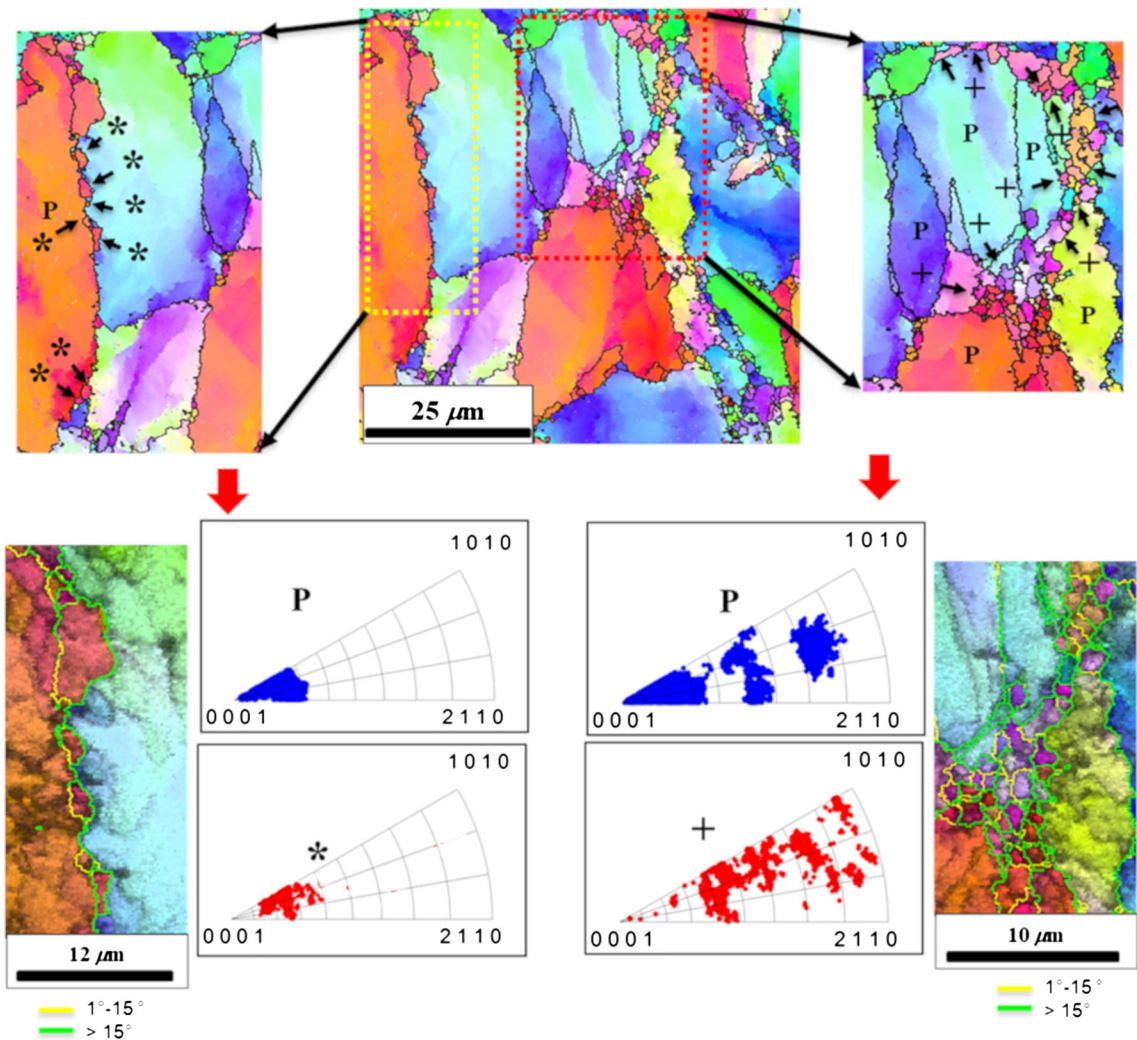


Fig. 10—Presence of two different (based on spatial location) types of DRx grains. The “\*” grains were located at the boundary of large deformed grains, while the “+” grains were in a classical necklace structure. The IPF plots show the \* and + grains and their suspected parent (P). The image was taken from 973K deformed sample A, but such observations were valid for other deformation conditions as well.

equiaxed grains. This was confirmed with TEM plus TKD (Figure 7) measurements. Finally, local internal friction measurements (Figure 11) provided a novel possibility for a clear demarcation between different microstructural features including identification of discontinuous DRx grains. The subsequent discussion of this manuscript is centered around (i) possible mechanism(s) of ‘limited’ DRx in  $\alpha$ -Zr and (ii) internal friction measurements as a potential tool for advanced microstructural characterization.

DRx in metallic materials, especially in fcc copper and austenitic iron,<sup>[14,66]</sup> has been associated with flow softening. Often the onset of DRx was detected prior to the peak stress by an inflection (softening) point.<sup>[66,67]</sup> This inflection of DRx is, however, opposite in nature to the inflection shown by deformation twinning.<sup>[68]</sup> For deformation twinning, there is an increase in the rate of strain hardening, while for the onset of DRx, there is a decrease. It is to be noted that the inflections seen in Figure 3 are all an increase. In other words, the non-cubic  $\alpha$ -Zr did not show (see Figures 2 and 3) typical

work softening associated with discontinuous DRx: especially discontinuous DRx reported<sup>[14,66,67,69]</sup> for cubic metallic materials. Hence, it seems appropriate to discuss possible conditions for associating discontinuous DRx with usually reported<sup>[10,14,15,66,67]</sup> work softening.

The first onset of DRx is usually observed at the inflection point,<sup>[10,14,15]</sup> at a strain less than that with the maximum stress. The maximum stress, on the other hand, is reported to require a finite fraction of dynamically recrystallized grains. Prior to the maximum in stress, there remains some residual work hardening with  $\frac{d\sigma}{de} > 0$ .<sup>[15,16]</sup> The new grains are expected to form with low dislocation densities. Thus, they are expected to be soft initially, but with an increased flow stress ( $\sigma_F$ ). The latter can be attributed to the Hall–Petch (HP) strengthening, see Eq. [3], from very small initial grain size.

$$\sigma_F = \sigma_0 + \frac{k_y}{\sqrt{d}} \quad [3]$$

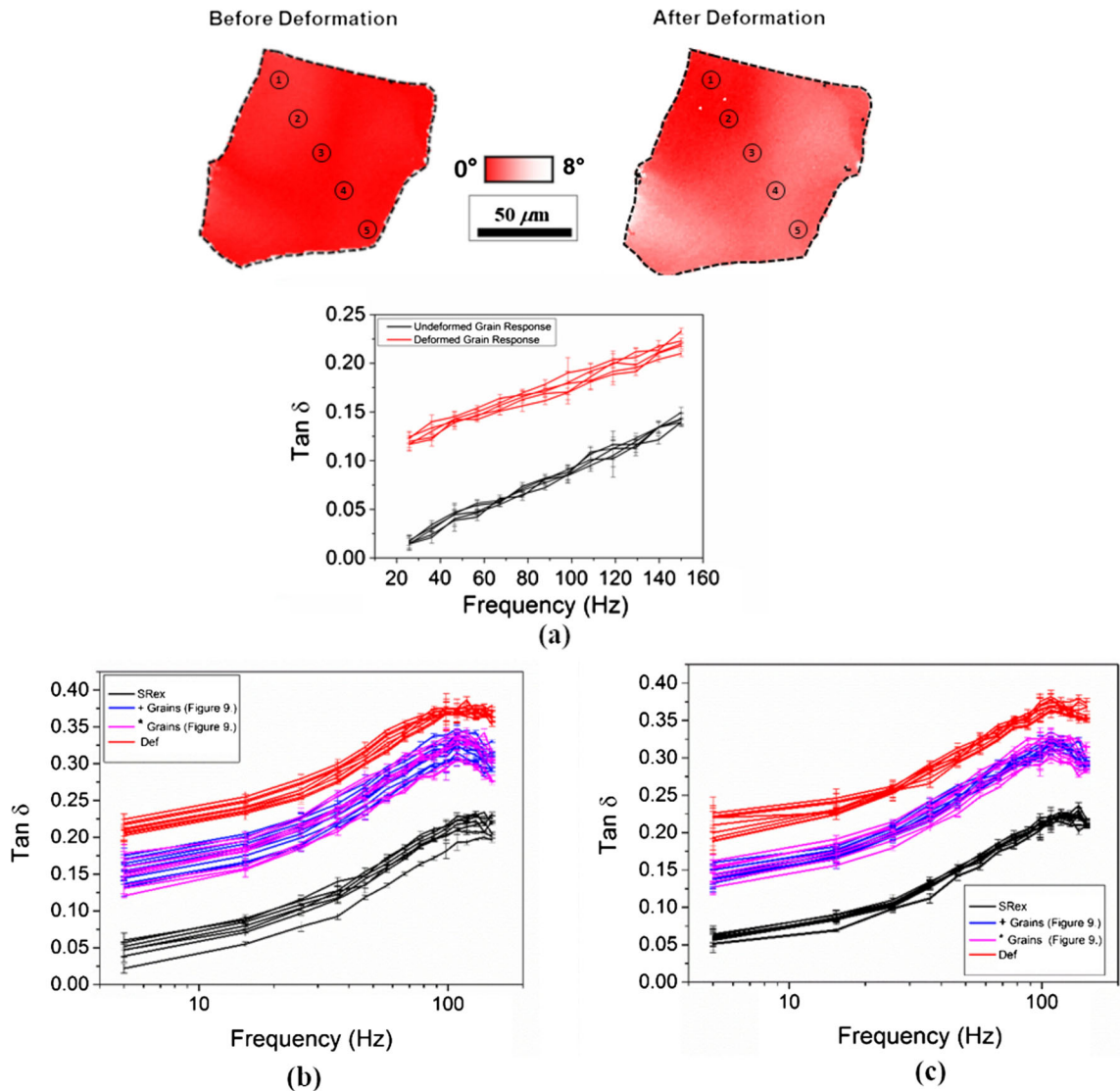


Fig. 11—(a) Internal friction ( $\tan\delta$ ) measurements for the same basal (0002) grain before and after room temperature tensile deformation (with about 5 pct imposed strain). These were made for the locations indicated in the figure. The figure shows developments of orientation gradients plus clear shift in  $\tan\delta$ . Also included,  $\tan\delta$  measurements for different microstructural features for (b) Basal (0002) and (c) Non-Basal (1120) orientations. The microstructural features included statically recrystallized grains (SRex), deformed ( $> 5 \mu\text{m}$  grains) and fine equiaxed grains (\* and + grains – as in Fig. 10). Figures (b) and (c) show randomly selected grains from 973 K deformed sample A. However, such observations were valid for other deformation conditions as well.

The high temperature of the HP hardening parameter is known to be smaller than the room temperature value.<sup>[55]</sup> With increasing hot deformation strain, several aspects of microstructural evolution are expected. The size of the initial grains will grow lowering their HP strengthening. These grains will also start to deform acquiring dislocations and thus becoming harder. During conventional recrystallization, the recrystallized fraction,  $X_R$ , will increase with time. This is likely to follow the standard nucleation and growth kinetics of Eq. [4].<sup>[66]</sup>

$$X_R = 1 - \exp(-At^n) \quad [4]$$

$$X_R = 1 - \exp(-A^* \varepsilon^{*n}) \quad [4a]$$

During discontinuous DRx, the time  $t$  can be replaced by extra strain (as in Eq. [4a])  $\varepsilon^*$ —representing strain beyond the onset of DRx. The nucleation and growth parameter  $A$  will become  $A^* = A(d\varepsilon/dt)^n$ . In the usual case where  $n > 1$ , an acceleration of the rate of growth of the softer fraction recrystallized ( $X_R$ ) will take place. If the new DRx grains have an average flow strength ( $\sigma_{FR}$ ), less than the flow stress of the un-recrystallized deformed grains ( $\sigma_D$ ) with its strain hardening ( $(d\sigma/d\varepsilon)_{DRx}$ ), then just after the maximum flow stress–work softening is expected.

$$\frac{dX_R}{d\varepsilon}(\sigma_D - \sigma_{FR}) > (1 - X_R) \left( \frac{d\sigma}{d\varepsilon} \right)_{DRx} \quad [5]$$

DRx grains in hot compressed  $\alpha$ -Zr grew very slowly. They were less than 5  $\mu\text{m}$  even after strains as high as 0.4. They also provided ‘limited’ area fraction (10 to 20 pct), see Figure 5(b). In addition, the hardness of these small DRx grains (at least at room temperature) significantly overlapped that of the deformed grains (Figure 9). The absence of work softening by the limited DRx (in the  $\alpha$ -Zr) is thus not very surprising.

The DRx in  $\alpha$ -Zr was ‘limited’ in the grain size. The rate of the DRx was also small, especially as compared to hot deformed fcc copper.<sup>[10,14]</sup> Two features of the deformed  $\alpha$ -Zr seem relevant. Firstly, extensive dynamic recovery,<sup>[70]</sup> as revealed by the stress–strain plots, was noted at or above 823 K. The ease of recovery appeared to be supported by the low activation energy for hot deformation.<sup>[23]</sup> As shown in Figure 2(d), 823 K to 1123 K hot compression with ‘limited’ DRx had an apparent activation energy of only  $140 \pm 15$  kJ/mole. Deformation at temperatures from 298 K to 723 K, on the other hand, provided a much higher activation energy of  $250 \pm 20$  kJ/mole. It is important to note that the activation energies for self-diffusion in  $\alpha$ -Zr were also reported, Perez *et al.*<sup>[39]</sup> and Horvat *et al.*,<sup>[71]</sup> to vary in a similar manner. This was estimated to be 115 and 350 kJ/mole for temperatures above and below 900 K, respectively. This has been attributed to the presence of ultra-fast diffusing elements such as iron. Irrespective of its origin, lower activation energy of  $\alpha$ -Zr appears to explain easy dynamic recovery.

Irrespective of its origin, lower activation energy of  $\alpha$ -Zr appears to explain easy dynamic recovery. It is expected that the mobility of the Zr atoms controls the dislocation recovery by vacancy migration. A further feature of the deformed  $\alpha$ -Zr, Figure 4(a), is the fragmentation of near grain boundary regions. Grain fragmentation, during plastic deformation, took place through realignment and recovery of dislocations and creation of high-angle boundaries.<sup>[65]</sup> The prior grain boundary fragmented regions appeared to act as the source for the DRx grains: a combination of stored energy and mobility advantage.<sup>[9,14]</sup> However, the well-recovered non-fragmented grains clearly ‘restricted’ the extent of the DRx. Thus, the inhibition of further DRX can be explained from continuing plastic deformation of the fine DRx grains plus growth inhibition through the non-fragmented grains of significantly lower stored energy. All these features of the hot deformed  $\alpha$ -Zr may account for the combination of both ‘limited’ DRx and the absence of any noticeable work softening.

Bulk internal friction measurements, in metallic materials, have attracted scientific interests before 1950. C.A. Zener, a physicist by training but a physical metallurgist by passion, was a strong proponent of internal friction measurements in characterizing aspects ranging from elastic anisotropy<sup>[40]</sup> and solute-point defect plus solute–solute interaction.<sup>[72,73]</sup> Zener also explored the potentials of internal friction by studying the role of grain size,<sup>[72]</sup> plastic deformation,<sup>[74]</sup> and

residual stresses.<sup>[75]</sup> Post-Zener research articles on internal friction are less abundant. Bulk internal friction measurements were related to identify possible sources of the mechanical relaxation<sup>[76]</sup>; subjects ranging from dislocation structure evolution,<sup>[77]</sup> phase transformation,<sup>[78]</sup> localized deformation,<sup>[79]</sup> and point defect interaction.<sup>[80]</sup> As the measurements were for a bulk quantity (loss or storage modulus, and their ratio or  $\tan\delta$  values<sup>[72]</sup>) and were not obtained on a specific microstructural feature they were less attractive to a typical metallurgist. The advent of nano-indentation,<sup>[28,81]</sup> quasi-static measurement of local load–displacement behavior, has brought interesting possibilities to materials characterization. More recently,<sup>[82]</sup> nano-indentation was adopted for the ac mode, where force and displacement can be modulated. These bring in the possibility of exploring dynamic mechanical properties such as internal friction. Of course, internal friction measurements with a nano-indenter have limitations. They can only be used for a narrow frequency range, and coupling such measurements with temperature can be a challenge.

The acoustical spectrum of a typical metal was studied by Zener *et al.*<sup>[61]</sup> Each peak in the spectrum corresponds to a particular type of relaxation.<sup>[40,61,72–80]</sup> More specifically, the preferred distribution of solute atoms in the z-type positions leads to the relaxation phenomenon, which takes place under an imposed stress. The solute atoms (example: carbon in iron) continually strive to reach their equilibrium position(s) under variable stress condition. The presence of point defects, dislocations, or residual stress may act as a barrier to such effort (of solute atoms in reaching respective equilibrium configurations), and hence reflect on the ‘relaxation’ during cyclic deformation. Apart from the dislocation configuration, the magnitude of dislocations or dislocation density appears to provide critical influence on the relaxation peak.<sup>[83]</sup> In reality, dislocations and stress coexist in deformed lattices,<sup>[54]</sup> and hence a combined effect is expected on the internal friction response. In plastic deformation, an individual grain does not deform homogeneously but a finite slip occurs across certain planes. After slipping, the two sides of a plane may not join together perfectly. The crystal structure may be broken down to a depth of several atomic distances. At best there are regions of misfit along the plane. With imperfections, it is reasonable to assume that dislocations render it impossible for certain areas to maintain a shearing stress permanently. But the relaxation of shearing stress across an area must also be accompanied by a partial relaxation of stress on either side of the area, and hence throughout a finite volume. Thus, each area which cannot permanently maintain a shearing stress contributes to the formation of a relaxation center. All these signify possible application of localized internal friction measurements in identifying different features of deformed microstructure. And this is exactly what has been achieved in this manuscript.

The internal friction values are biased by several possible events<sup>[40,72–75]</sup> and decoupling them experimentally might be difficult. More specifically, even in a

slightly deformed grain of hexagonal Zr (see Figure 11(a)), the nano-dma values changed with spatial location. This can be attributed to the generation of both local dislocations and point defects (through plastic deformation) and changes in the state of local residual stress. The authors believe an atomistic simulation, such as molecular dynamics (MD), might be effective in capturing (and decoupling) such effects. However, there are limited publications on internal friction plus MD in metallic material.<sup>[84,85]</sup> Though our initial efforts (at MD simulations) show that local  $\tan\delta$  values are sensitive to the aforementioned features (point defects, dislocations as well as lattice strain), there are certain limitations. Not only are the simulation volumes extremely small, MD time scale leads to a dma frequency range of  $\sim 10^{12} \text{ s}^{-1}$ , much higher than those achievable by experiments. It is believed that MD plus Kinetic Monte Carlo (KMC) may offer a more realistic solution, but such possibilities are for the future.

## V. CONCLUSIONS

Fully recrystallized hexagonal zirconium ( $\alpha$ -Zr), of two distinct crystallographic textures, was subjected to controlled warm/hot compression tests in a deformation simulator. Following were the main observations:

- (1) The stress-strain behavior showed strain hardening and flow saturation below and above 723K, respectively. Though flow saturation typically indicates dynamic recovery, fine equiaxed grains, often indicative of dynamic recrystallization (DRx), were observed in samples deformed  $> 723 \text{ K}$ . Combined TKD (transmission Kikuchi diffraction) plus TEM (transmission electron microscopy) measurements showed clear presence of orientation gradients and dislocations inside the fine equiaxed grains. It is hence apparent the discontinuous DRx happened in  $\alpha$ -Zr without visible flow softening. 'Limited' ( $0.25 \leq$  in area fraction and below  $5 \mu\text{m}$  in grain size) DRx with relatively insignificant work softening appears to be characteristic of hot deformed  $\alpha$ -Zr.
- (2) Microtexture measurements, at smaller step size, revealed two types of DRx grains. Grains existing at the boundaries of deformed grains appeared to be growing by SIBM (strain-induced boundary migration). The other type of DRx grains had the typical necklace-type structures. However, grain interior misorientations or local mechanical properties (nano-hardness) could not distinguish between different microstructural features or demarcate DRX grains (of two different types) from deformed and statically recrystallized (SRex) grains.
- (3) Local internal frictional measurements, or  $\tan\delta$  vs frequency (5 to 150 Hz), had identical and reproducible values inside individual SRex grain(s). However,  $\tan\delta$  was extremely sensitive to even minor plastic deformation, a possible effect of dislocations and point defects plus

residual stress evolution. Though demarcating the effect of different parameters on  $\tan\delta$  remains pending, the study clearly established the ability of local internal friction measurements in distinguishing between different microstructural features, and being a novel tool for the identification of the DRx grains.

## ACKNOWLEDGMENTS

The authors would like to acknowledge BRNS (board of research on nuclear sciences, India) for support. Support from SERB-DST (science and engineering research board – department of science and technology, India) and the National Facility of Texture and OIM (IIT Bombay) are also acknowledged. RDD also acknowledges support from IIT Bombay as a visiting professor.

## REFERENCES

1. K.L. Murty and I. Charit: *Prog. Nucl. Energy*, 2006, vol. 48, pp. 325–59.
2. P. Rudling and B. Kammenzind: *Zirconium in the Nuclear Industry: Fourteenth International Symposium*, 2005.
3. N. Saibaba: *J. Nucl. Mater.*, 2008, vol. 383, pp. 63–70.
4. R.G. Ballinger, G.E. Lucas, and R.M. Pelloux: *J. Nucl. Mater.*, 1984, vol. 126, pp. 53–69.
5. K.V.M. Krishna, S.K. Sahoo, I. Samajdar, S. Neogy, R. Tewari, D. Srivastava, G.K. Dey, G.H. Das, N. Saibaba, and S. Banarjee: *J. Nucl. Mater.*, 2008, vol. 383, pp. 78–85.
6. M.R. Daymond, R.A. Holt, S. Cai, P. Mosbrucker, and S.C. Vogel: *Acta Mater.*, 2010, vol. 58, pp. 4053–66.
7. D.L. Bourell and H.J. McQueen: *J. Mater. Shap. Technol.*, 1987, vol. 5, pp. 53–73.
8. H. Abe, T. Iwamoto, Y. Yamamoto, S. Nishida, and R. Komatsu: *J. Mater. Process. Technol.*, 2016, vol. 231, pp. 277–87.
9. B. Verlinden, J. Driver, I. Samajdar, and R.D. Doherty: *Thermo-Mechanical Processing of Metallic Materials*, Elsevier, Amsterdam, 2007, vol. 11.
10. H.J. McQueen and J.J. Jonas: *Recovery and Recrystallization During High Temperature Deformation*, Academic Press Inc, New York, 1975, vol. 6.
11. H.J. McQueen and J.J. Jonas: *J. Appl. Metalwork.*, 1984, vol. 3, pp. 233–41.
12. T. Sakai, A. Belyakov, R. Kaibyshev, H. Miura, and J.J. Jonas: *Prog. Mater. Sci.*, 2014, vol. 60, pp. 130–207.
13. K. Huang and R.E. Logé: *Mater. Des.*, 2016, vol. 111, pp. 548–74.
14. F.J. Humphreys and M. Hatherly: *Recrystallization and Related Annealing Phenomena*/F.J. Humphreys and M. Hatherly, 1st ed., Pergamon Oxford, UK, 1995.
15. G. Gottstein, M. Frommert, M. Goerdeler, and N. Schäfer: *Mater. Sci. Eng. A*, 2004, vol. 387, pp. 604–08.
16. E.I. Poliak and J.J. Jonas: *Acta Mater.*, 1996, vol. 44, pp. 127–36.
17. B. Luan, S. Gao, L. Chai, X. Li, A. Chapuis, and Q. Liu: *Mater. Des.*, 2013, vol. 52, pp. 1065–70.
18. C. Chauvy, P. Barberis, and F. Montheillet: *Mater. Sci. Eng. A*, 2006, vol. 431, pp. 59–67.
19. S.R. Barrabes, M.E. Kassner, M.T. Pérez-Prado, and E. Evangelista: *Mater. Sci. Forum*, 2004, vols. 467–470, pp. 1145–50.
20. M.T. Pérez-Prado, S.R. Barrabes, M.E. Kassner, and E. Evangelista: *Acta Mater.*, 2005, vol. 53, pp. 581–91.
21. R. Kapoor, G.B. Reddy, and A. Sarkar: *Mater. Sci. Eng. A*, 2018, vol. 718, pp. 104–10.
22. J.K. Chakravarty, R. Kapoor, A. Sarkar, S. Banerjee, P. Barberis, and S.W. Dean: *J. ASTM Int.*, 2010, vol. 7, pp. 1–17.

23. L.Y. Qian, G. Fang, P. Zeng, and L.X. Wang: *Int. J. Press. Vessel. Pip.*, 2015, vols. 132–133, pp. 43–51.
24. S.I. Wright, M.M. Nowell, and D.P. Field: *Microsc. Microanal.*, 2011, vol. 17, pp. 316–29.
25. H. Mirzadeh, J.M. Cabrera, A. Najafizadeh, and P.R. Calvillo: *Mater. Sci. Eng. A*, 2012, vol. 538, pp. 236–45.
26. N. Srinivasan, V. Kain, N. Birbilis, K.V. Mani Krishna, S. Shekhawat, and I. Samajdar: *Corros. Sci.*, 2015, vol. 100, pp. 544–55.
27. GC Sneddon, PW Trimby, and JM Cairney: *Mater. Sci. Eng.*, 2016, vol. 110, pp. 1–12.
28. G.M. Pharr: *J. Mater. Res.*, 1992, vol. 7, pp. 1564–83.
29. A.C. Fischer-Cripps: *Nanoindentation*, Springer, New York, 2004.
30. S.R. Cohen and E. Kalfon-Cohen: *Beilstein J. Nanotechnol.*, 2013, vol. 4, pp. 815–33.
31. S. Bhowmick, S. Ozden, R.A. Bizão, L.D. Machado, S.A.S. Asif, N.M. Pugno, D.S. Galvão, C.S. Tiwary, and P.M. Ajayan: *Carbon N. Y.*, 2019, vol. 142, pp. 291–99.
32. A Durgaprasad, S Giri, S Lenka, S Kundu, S Mishra, S Chandra, RD Doherty, and I Samajdar: *Metall. Mater. Trans. A*, 2017, vol. 48A, pp. 4583–97.
33. S. Bhowmick, Z. Alam, and S.A.S. Asif: *Microsc. Microanal.*, 2016, vol. 22, pp. 1740–41.
34. B.B. He: *Two-Dimensional X-Ray Diffraction*, Wiley, Hoboken, NJ, 2009.
35. B Leiss, K Ullemeyer, and K Weber: *J. Struct. Geol.*, 2000, vol. 11, pp. 1527–29.
36. KV Mani Krishna, R Raghavan, D Srivastava, GK Dey, SK Sahoo, and I Samajdar: *Trans. Indian Inst. Met.*, 2011, vol. 64, pp. 309–13.
37. V.D. Hiwarkar, S.K. Sahoo, I. Samajdar, A. Satpathy, K.V.M. Krishna, G.K. Dey, D. Srivastav, R. Tewari, and S. Banarjee: *J. Nucl. Mater.*, 2011, vol. 412, pp. 287–93.
38. E. El-Danaf, S.R. Kalidindi, and R.D. Doherty: *Metall. Mater. Trans. A*, 1999, vol. 30A, pp. 1223–33.
39. R.A. Perez, H. Nakajima, and F. Dymment: *Mater. Trans.*, 2003, vol. 44, pp. 2–13.
40. C. Zener: *Phys. Rev.*, 1938, vol. 53, pp. 90–99.
41. RJ McCabe, EK Cerreta, A Misra, GC Kaschner, and CN Tomé: *Philos. Mag.*, 2006, vol. 86, pp. 3595–611.
42. G.C. Kaschner, C.N. Tomé, I.J. Beyerlein, S.C. Vogel, D.W. Brown, and R.J. McCabe: *Acta Mater.*, 2006, vol. 54, pp. 2887–96.
43. J. Singh, S. Mahesh, S. Roy, G. Kumar, D. Srivastava, G.K. Dey, N. Saibaba, and I. Samajdar: *Acta Mater.*, 2017, vol. 123, pp. 337–49.
44. A. Akhtar: *Acta Metall.*, 1973, vol. 21, pp. 1–11.
45. A.D. Rollett and U.F. Kocks: *Solid State Phenom.*, 1993, vols. 35–36, pp. 1–18.
46. SK Sahoo, VD Hiwarkar, KV Mani Krishna, I Samajdar, P Pant, PK Pujari, GK Dey, D Srivastav, R Tiwari, and S Banerjee: *Mater. Sci. Eng. A*, 2010, vol. 527, pp. 1427–35.
47. N Keskar, S Mukherjee, KV Mani Krishna, D Srivastava, GK Dey, P Pant, RD Doherty, and I Samajdar: *Acta Mater.*, 2014, vol. 69, pp. 265–74.
48. SI Wright: *J. Comput. Microsc.*, 1993, vol. 5, pp. 207–21.
49. A. Hadadzadeh, F. Mokdad, M.A. Wells, and D.L. Chen: *Mater. Sci. Eng. A*, 2018, vol. 709, pp. 285–89.
50. H-J Bunge: *Texture Analysis in Materials Science*, Elsevier, Amsterdam, 1982, pp. 351–403.
51. M.M. Nowell and S.I. Wright: *Ultramicroscopy*, 2005, vol. 103, pp. 41–58.
52. S.I. Wright, M.M. Nowell, S.P. Lindeman, P.P. Camus, M. De Graef, and M.A. Jackson: *Ultramicroscopy*, 2015, vol. 159, pp. 81–94.
53. M.H. Alvi, S.W. Cheong, H. Weiland, and A.D. Rollett: *Mater. Sci. Forum*, 2004, vols. 467–470, pp. 357–62.
54. A. Lodh, I. Samajdar, R. Tewari, D. Srivastava, G.K. Dey, and P. Pant: *Mater. Sci. Forum*, 2011, vols. 702–703, pp. 311–14.
55. S.V. Ramani and P. Rodriguez: *Can. Met. Q.*, 1972, vol. 11, pp. 61–67.
56. Y. Yogo, H. Takeuchi, T. Ishikawa, N. Iwata, and K. Nakanishi: *Scr. Mater.*, 2009, vol. 61, pp. 1001–03.
57. TS Prithiv, P Bhuyan, SK Pradhan, V Subramanya Sarma, and S Mandal: *Acta Mater.*, 2018, vol. 146, pp. 187–201.
58. A. Dehghan-Manshadi, M. Barnett, and P. Hodgson: *Metall. Mater. Trans. A*, 2008, vol. 39A, pp. 1359–70.
59. C. Zener: *Physica*, 1949, vol. 15, pp. 111–18.
60. E.J. Savino and E.A. Bisogni: *J. Nucl. Mater.*, 1974, vol. 50, pp. 298–308.
61. A.J. Bedford, P.G. Fuller, and D.R. Miller: *J. Nucl. Mater.*, 1972, vol. 43, pp. 164–74.
62. L.T. Miyada-Naborikawa and R. De Batist: *Phys. Status Solidi*, 1985, vol. 191, pp. 191–98.
63. T.O. Erinoshio and F.P.E. Dunne: *Int. J. Plast.*, 2015, vol. 71, pp. 170–94.
64. T.M. Poletika, G.N. Narimanov, and S.V. Kolosov: *J. Appl. Mech. Tech. Phys.*, 2003, vol. 44, pp. 262–70.
65. S.K. Sahoo: Ph. D. Thesis: Heterogeneous deformation in zirconium-based alloys, 2009, Indian Institute of Technology, Bombay.
66. A.A. Salem, S.R. Kalidindi, and R.D. Doherty: *Acta Mater.*, 2003, vol. 51, pp. 4225–37.
67. C. Chauvy, P. Barbéris, and F. Montheillet: *Mater. Sci. Forum*, 2004, vols. 467–470, pp. 1151–56.
68. H. Hallberg, M. Wallin, and M. Ristinmaa: *Comput. Mater. Sci.*, 2010, vol. 49, pp. 25–34.
69. S.H. Zahirri, C.H.J. Davies, and P.D. Hodgson: *Scr. Mater.*, 2005, vol. 52, pp. 299–304.
70. T. Sakai and J.J. Jonas: *Acta Metall.*, 1984, vol. 32, pp. 189–209.
71. J. Horváth, F. Dymment, and H. Mehrer: *J. Nucl. Mater.*, 1984, vol. 126, pp. 206–14.
72. C. Zener: *Phys. Rev.*, 1947, vol. 71, pp. 34–38.
73. A.H. Barnes and C. Zener: *Phys. Rev.*, 1940, vol. 58, pp. 87–87.
74. C. Zener and J.H. Hollomon: *J. Appl. Phys.*, 1946, vol. 17, pp. 69–82.
75. C. Zener: *Phys. Rev.*, 1941, vol. 60, pp. 455–57.
76. F. Povoletto and E.A. Bisogni: *Acta Metall.*, 1967, vol. 15, pp. 701–06.
77. R. den Burman and A.P. Snoep: *Acta Metall.*, 1972, vol. 20, pp. 407–13.
78. J.E. Doherty and D.F. Gibbons: *Acta Metall.*, 1971, vol. 19, pp. 275–82.
79. L. Parrini and R. Schaller: *Acta Mater.*, 1996, vol. 44, pp. 4881–88.
80. R.R. Hasiguti, N. Igata, and G. Kamoshita: *Acta Metall.*, 1962, vol. 10, pp. 442–47.
81. CA Schuh: *Nanoindentation Stud. Mater.*, 2006, vol. 9, pp. 32–40.
82. R. Foschia, M. Jobin, and S. Hengsberger: *Micron*, 2009, vol. 40, pp. 51–55.
83. P.P. Pal-val, M. Hamersky, Z. Trojanova, and P. Lukac: *Phys. Status Solidi*, 1991, vol. 13, pp. 13–16.
84. S. Feng, L. Qi, F. Zhao, S. Pan, G. Li, M. Ma, and R. Liu: *J. Mater.*, 2015, vol. 80, pp. 36–40.
85. Y Kogure, T Kosugi, T Nozaki, and M Doyama: *Mater. Sci. Eng. A*, 2009, vol. 521, pp. 30–33.

**Publisher's Note** Springer Nature remains neutral with regard to jurisdictional claims in published maps and institutional affiliations.